

X-ray diffraction microscopy based on refractive optics

Thomas Roth*, Carsten Detlefs, Irina Snigireva, Anatoly Snigirev

European Synchrotron Radiation Facility,
B.P. 220, 6 rue Jules Horowitz, 38043 Grenoble Cedex 9, France

September 21, 2014

Keywords: Diffraction imaging, X-ray microscopy, Compound refractive lenses, X-ray topography

Abstract

We describe a diffraction microscopy technique based on refractive optics to study structural variations in crystals. The X-ray beam diffracted by a crystal was magnified by Beryllium parabolic refractive lenses on a 2D X-ray camera. The microscopy setup was integrated into the 6-circle Huber diffractometer at the ESRF beamline ID06. Our setup allowed us to visualize structural imperfections with a resolution of $\approx 1 \mu\text{m}$. The configuration, however, can easily be adapted for sub- μm resolution.

1 Introduction

X-ray diffraction imaging, known later as X-ray topography, originated in the late 1920ies and early 1930ies, when researchers revealed the internal structure of individual Laue spots in diffraction patterns [1, 2]. To improve the resolution, fine grain photographic emulsions were exposed and examined under optical microscopes – for this reason the technique was sometimes called X-ray microscopy [3]. This method was applied for both mapping of strains in heavily deformed materials such as cold-worked metals and alloys [3] and studies of individual defects in near-perfect single crystals [4].

It was assumed that each point on the film or detector corresponds to a small volume in the reflecting crystal. Simple geometrical optics then requires the incoming X-ray beam to be tightly collimated, and the film to be placed as closely as possible to the sample. The achievable resolution is then limited by the detector resolution, at best 500 nm [5] but more typically $1 \mu\text{m}$.

However, in the absence of X-ray optics between the sample and the film diffraction effects progressively blur the image with increasing sample-to-detector distance. For a typical experimental setup (wavelength $\lambda = 1 \text{ \AA}$, sample-to-detector distance $s = 1 \text{ cm}$, and sample feature size $d = 1 \mu\text{m}$) the diffraction limited resolution due to propagation of the perturbed wavefront from the exit surface of the crystal to the detector can be approximated as

$$\delta \approx \frac{\lambda}{d} \cdot s = \frac{10^{-10} \text{ m}}{10^{-6} \text{ m}} \cdot 10^{-2} \text{ m} = 1 \mu\text{m}. \quad (1)$$

Note that to image $10\times$ smaller features on the sample ($d = 100 \text{ nm}$ and therefore $\delta = 100 \text{ nm}$) the sample-to-detector distance would have to be decreased by a factor of 100, $s = 100 \mu\text{m}$. In most cases this is technically not feasible. Furthermore, to the best of our knowledge, 2D imaging detectors with a spatial resolution of 100 nm are not yet available.

On the other hand, conventional X-ray microscopy techniques as proposed by Kirkpatrick and Baez [6, 7] have been implemented in the hard X-ray domain rather late. Here, an in-line scheme is used where the beam transmitted through the sample is magnified by X-ray optics such as mirrors [8], Fresnel zone plates [9],

*now at: European XFEL GmbH, Hamburg, Germany. e-mail: thomas.roth@xfel.eu

Bragg-Fresnel lenses [10], or refractive lenses [11]. Such forward scattering techniques are primarily sensitive to spatial variations of the X-ray index of refraction which depends mostly on the local density of the sample.

In this paper we propose a compact scheme for diffraction microscopy using X-ray refractive lenses between the sample and the detector. The insertion of refractive optics into the diffracted beam allows significant improvements of the resolution, potentially down to below 100 nm (a resolution of 300 nm has been demonstrated using a similar lens in transmission X-ray microscopy[12]). Furthermore, the progressive blurring due to the wavefront propagating from the sample to the detector can be overcome by a lens, thus reestablishing the direct mapping of intensity variations on the detector to the reflectivity variations on the sample. In this case the image resolution can, in principle, reach the limit imposed by dynamical diffraction effects within the crystal.

Recently, Fresnel zone plates have been used in X-ray reflection microscopy to image monomolecular steps at a solid surface [13] and for scanning X-ray topography of strained silicon oxide structures [14]. CRLs have the advantage that efficient focusing can be achieved at higher photon energies, $E \gg 10$ keV. Please note that standard KB mirrors are not suited for imaging setups, as they do not fulfill the Abbe-sine condition. More complicated multi-mirror setups are however being developed to overcome this limitation in transmission geometry [15].

2 Experimental details

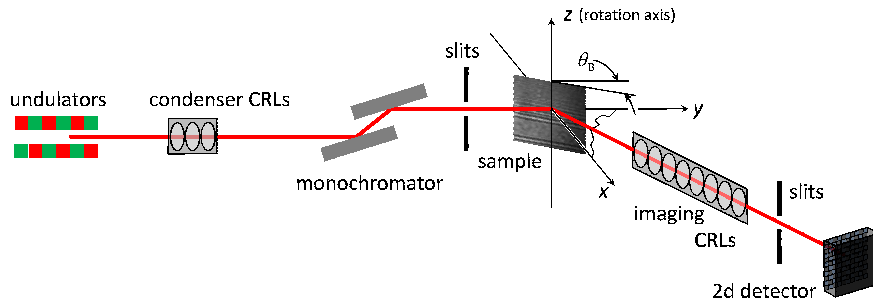


Figure 1: Experimental setup for Bragg diffraction microscopy. 11 keV X-rays impinge on the sample. The diffracted intensity is imaged onto a Sensicam camera via a set of 66 Beryllium compound refractive lenses (CRLs) with an apex-radius of curvature of $50 \mu\text{m}$. The scattering plane is horizontal, and the imaged features on the sample were aligned parallel to the scattering plane.

Our experiment was carried out at the undulator beamline ID06 of the European Synchrotron Radiation Facility. A cryogenically cooled permanent magnet in-vacuum undulator [16] with a period of 18 mm and a conventional in-air undulator with a period of 32 mm, combined with a liquid nitrogen cooled Si (111) monochromator, delivered photons at an energy of 11 keV. A transfocator located at 38.7 m from the source point (electron beam waist position in the middle between the two undulators) acted as a condenser, i.e. it focused the photons onto the sample at 67.9 m distance from the source, using a combination of paraboloid (2D) compound refractive lenses, CRLs, [11]: one lens with radius of curvature at the apex $R= 1.5$ mm and two lenses with $R= 0.2$ mm, all made out of high-purity Beryllium (Be). The use of the condenser-CRLs improved the optical efficiency of the system (absorption of X-rays in the condenser-CRLs was only about 6%), as it increased the flux on the imaged sample area. The divergence of the photon beam is not altered significantly, as the condenser CRL works almost in a 1:1 magnification geometry. A flux of approximately $2 \cdot 10^{12}$ photons/s was incident to the sample. The sample was mounted on a six circle diffractometer. The scattering plane coincided with the horizontal plane.

The detector consisted of a scintillator screen, magnifying optics, and a high resolution CCD-camera. The $9.9 \mu\text{m}$ thick LAG:Eu scintillator on a $170 \mu\text{m}$ YAG substrate converted X-rays into visible light, which

was projected onto the CCD by the objective lens (Olympus UPLAPO $\times 10$, numerical aperture 0.4). The CCD camera (pco SenciscamQE) had 1376×1040 pixels (px) of size $6.45 \mu\text{m}/\text{px} \times 6.45 \mu\text{m}/\text{px}$ and 12 bit depth, yielding a field of view on the scintillator of $887 \times 670 \mu\text{m}^2$ with an effective resolution of $1.3 \mu\text{m}$. Each CCD pixel imaged an area of $0.645 \times 0.645 \mu\text{m}^2$ on the scintillator.

In front of the detector, on the same diffractometer arm, a second set of paraboloid Be CRLs (66 lenses with apex-radius of curvature $R=50 \mu\text{m}$) was mounted as X-ray objective lens, i.e. to image the diffracted intensity pattern at the sample exit surface onto the detector. These lenses were mounted on translation and rotation stages to align the lens stack, in particular to tune the sample-to-lens distance to achieve best focusing onto the detector.

The focal length of this lens stack at 11 keV was about 14 cm, so that a ≈ 4 -fold magnified image was achieved with the lens center placed about 18 cm downstream of the sample. The effective aperture was about $240 \mu\text{m}$, giving a corresponding diffraction limit of 130 nm. The transmission through the lens stack is reduced by the absorption from the thinnest lens part, plus the increased absorption for rays travelling further away from the lens center, resulting in an effective aperture with Gaussian profile [10, 11]. The first contribution is easy to calculate and gives an absorption of 18%. Considering the size of the illuminated sample ($\approx 200 \text{ nm}$, see below) and approximating the reflected beam as a parallel beam, the total absorption is closer to 50%.

Scaling the effective detector resolution by the magnification factor 4 to $1.3 \mu\text{m}/4 = 0.33 \mu\text{m}$, we expected a resolution limit of $\sqrt{(0.33 \mu\text{m})^2 + (130 \text{ nm})^2} \approx 350 \text{ nm}$ with this set-up.

Two samples were imaged in Bragg geometry. The first sample was a Si (111) wafer upon which a regular stripe pattern of amorphous SiO_2 has been fabricated by thermal oxidation followed by standard photo-resist etching. The SiO_2 layer was $z = 1.15 \mu\text{m}$ thick, and was etched to fabricate $2 \mu\text{m}$ wide windows with a period of $4 \mu\text{m}$. The substrate was aligned in the diffractometer to set the oxide stripes parallel to the diffraction plane. In order to record magnified diffraction images of the sample the Bragg (333) reflection of the Si substrate (Bragg angle $\theta_B = 32.63^\circ$) was used.

The second sample was a linear Bragg-Fresnel lens (BFL) fabricated on a Si (111) substrate (for the fabrication process see [17]). The basic geometrical parameters were: an outermost zone width of $0.5 \mu\text{m}$, a height of the structure of $4.4 \mu\text{m}$, and an aperture of $200 \mu\text{m}$. Again, the sample was aligned with the structures parallel to the horizontal scattering plane. Again, the Si (333) ($\theta_B = 32.63^\circ$) reflection was studied.

3 Resolution

The homogeneous periodicity of the SiO_2 line pattern (Fig. 2) was used to calibrate the effective magnification of our configuration. The mask used to produce the pattern had a period of $4 \mu\text{m}$, in good agreement with the value, $4.1(1) \mu\text{m}$, obtained by scanning electron microscopy (SEM), see Fig. 2f. Our X-ray image of this structure shows 15 periods over 395(5) px. (Fig. 2b) The line spacing on the fluorescence screen of the detector was therefore $0.645 \mu\text{m}/\text{px} \cdot 395 \text{ px}/15 = 17.0(2) \mu\text{m}$, yielding a magnification factor of $17.0 \mu\text{m}/4.1 \mu\text{m} = 4.2(1)$ for the CRL stack and $4.1 \mu\text{m} \cdot 15/395 \text{ px} = 0.156(4) \mu\text{m}/\text{px}$ for the overall experiment. The resulting field of view on the sample was $\approx 162 \mu\text{m}/\sin(\theta_B)$ in the horizontal (within the scattering plane) and $215 \mu\text{m}$ in the vertical direction (perpendicular to the scattering plane).

An upper limit for the effective resolution of our imaging system can be estimated from the Fourier transform (FT) of the image (see Fig. 3). Peaks corresponding to the fundamental, second and third harmonics of the structure are clearly visible above a two-component background. For quantitative analysis, the FT was fitted to a model function

$$\tilde{I}(f) = \sum_{n=1}^3 (A_n \cdot g(f - n f_1)) + a e^{-f/f_{\text{BG}}} + b, \quad (2)$$

where $\tilde{I}(f)$ is the Fourier transform of the image at spatial frequency f . The background is composed of a constant and an exponentially decaying term with characteristic frequency f_{BG} . The harmonics are

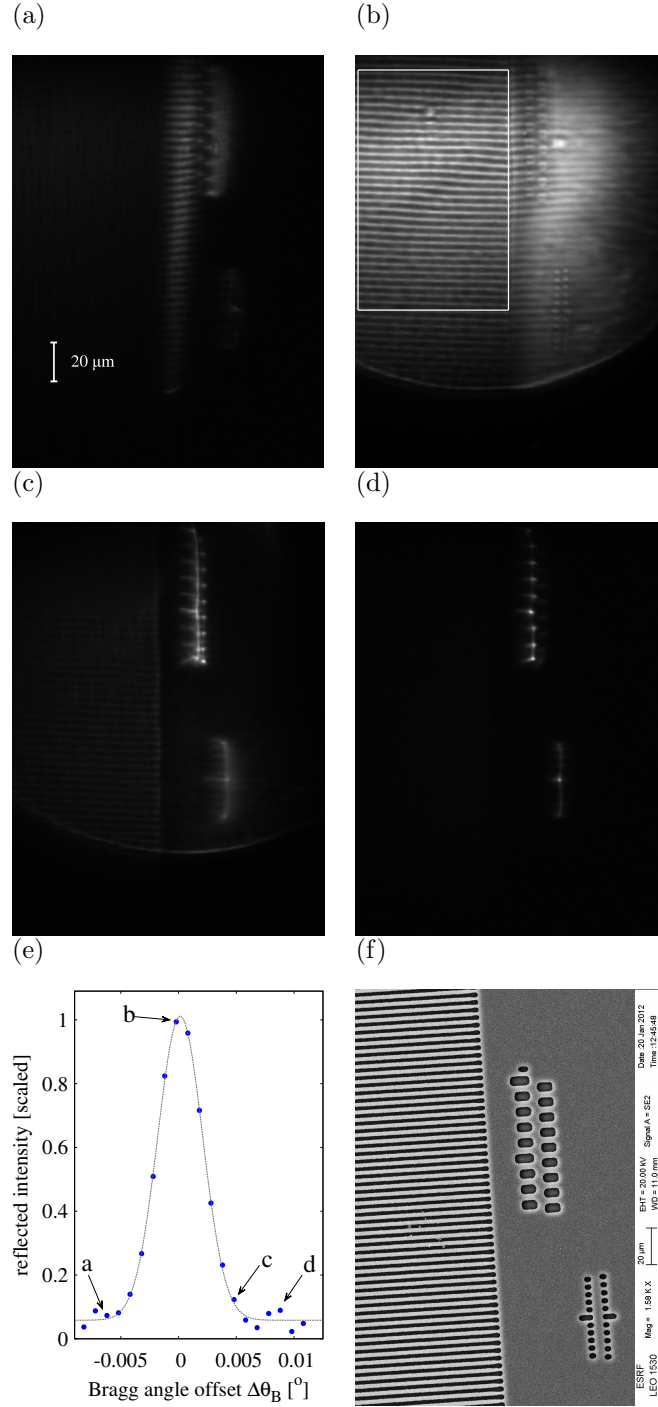


Figure 2: Diffraction microscopy images (exposure time 2.5 s) of the SiO_2 stripe structure at different Bragg angles: a) at 0.006° below the maximum diffracted intensity; b) almost at the maximum; c) 0.005° above the maximum; d) 0.009° above the maximum. The beam travels from left to right. e) Rocking curve as measured by a photo diode, indicating also the angle positions corresponding to Figs. 2a) to 2d). f) Scanning electron microscope image of the same SiO_2 stripe system. Note that b) shows stripe like intensity in a region where e) shows a homogeneous SiO_2 surface. This indicates a strain propagation in the Si beyond the etched areas.

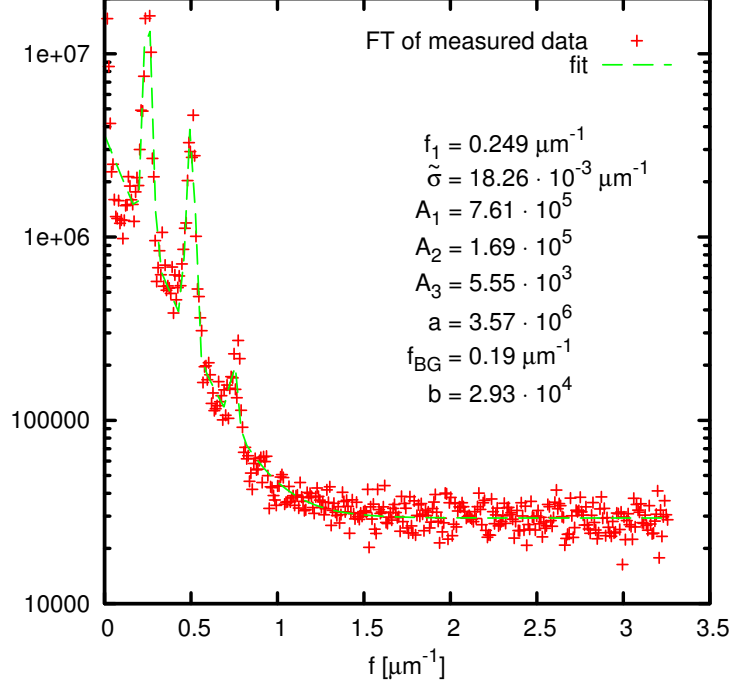


Figure 3: Fourier transform of the diffraction microscopy image shown in Fig. 2(b). The region of interest was divided into 10 vertical slices. The data shown here represent the magnitude of the Fourier transform averaged over these 10 slices. The parameters listed are the result of a fit to eq. 2.

modelled by Gaussians $g(f) = (2\pi\tilde{\sigma}^2)^{-1/2} \exp(-f^2/2\tilde{\sigma}^2)$ with amplitude factors A_n for the n -th harmonic. The magnification factor determined above ($0.156 \mu\text{m}/\text{px}$) was used to scale the frequency axis. The resulting parameters are shown in Fig. 3. The ratio A_1/A_3 can be used to estimate the modulation transfer function (MTF), $\tilde{I}(f) = \tilde{c}(f) \cdot \text{MTF}(f)$, where $\tilde{c}(f)$ is the FT of the scattering amplitude of the sample. For an ideal square wave, $\tilde{c}(f_1)/\tilde{c}(3f_1) = 3$. For a more smooth modulation, e.g. resulting from continuous buckling of the Bragg planes due to strain [18], the higher harmonics will be suppressed, $\tilde{c}(f_1)/\tilde{c}(3f_1) > 3$ so that

$$\frac{\tilde{I}(f_1)}{\tilde{I}(3f_1)} = \frac{\tilde{c}(f_1)}{\tilde{c}(3f_1)} \cdot \frac{\text{MTF}(f_1)}{\text{MTF}(3f_1)} \geq 3 \cdot \frac{\text{MTF}(f_1)}{\text{MTF}(3f_1)} \quad (3)$$

The presence of a second harmonic at $2f_1$ indicates that the contrast does not follow an ideal square modulation.

In the absence of any further information, we assume the MTF to be a Gaussian with standard deviation $\tilde{\sigma}_{\text{MTF}}$, so that $\tilde{\sigma}_{\text{MTF}} = 2f_1 (\log[\text{MTF}(f_1)/\text{MTF}(3f_1)])^{-1/2}$. Using the values obtained from the fit we find $\tilde{\sigma}_{\text{MTF}} \geq 0.254 \mu\text{m}^{-1}$, corresponding to a Gaussian point spread function (PSF) with standard deviation $\tilde{\sigma}_{\text{PSF}} = 1/(2\pi\tilde{\sigma}_{\text{MTF}}) \leq 0.625 \mu\text{m}$ and full width at half maximum (FWHM) $\leq 1.47 \mu\text{m}$ on the sample (9.4 px on the CCD).

Further experiments were performed on a Bragg-Fresnel lens. In this sample, the zone width decreases away from the center, thus yielding a richer Fourier spectrum that should provide more detailed information on the MTF and the effective resolution of our system.

Fig. 4 shows the Bragg microscopy images of the Bragg-Fresnel lens (panels a and b), a Scanning electron microscopy image of the same structure (panel c), and a Fourier analysis (panel d) of the region of interest shown in panel b.

As above, Fourier analysis was performed to reveal the resolving power of our experiment. The region of interest shown in panel b) was divided into 10 vertical slices. Each slice was Fourier transformed, The

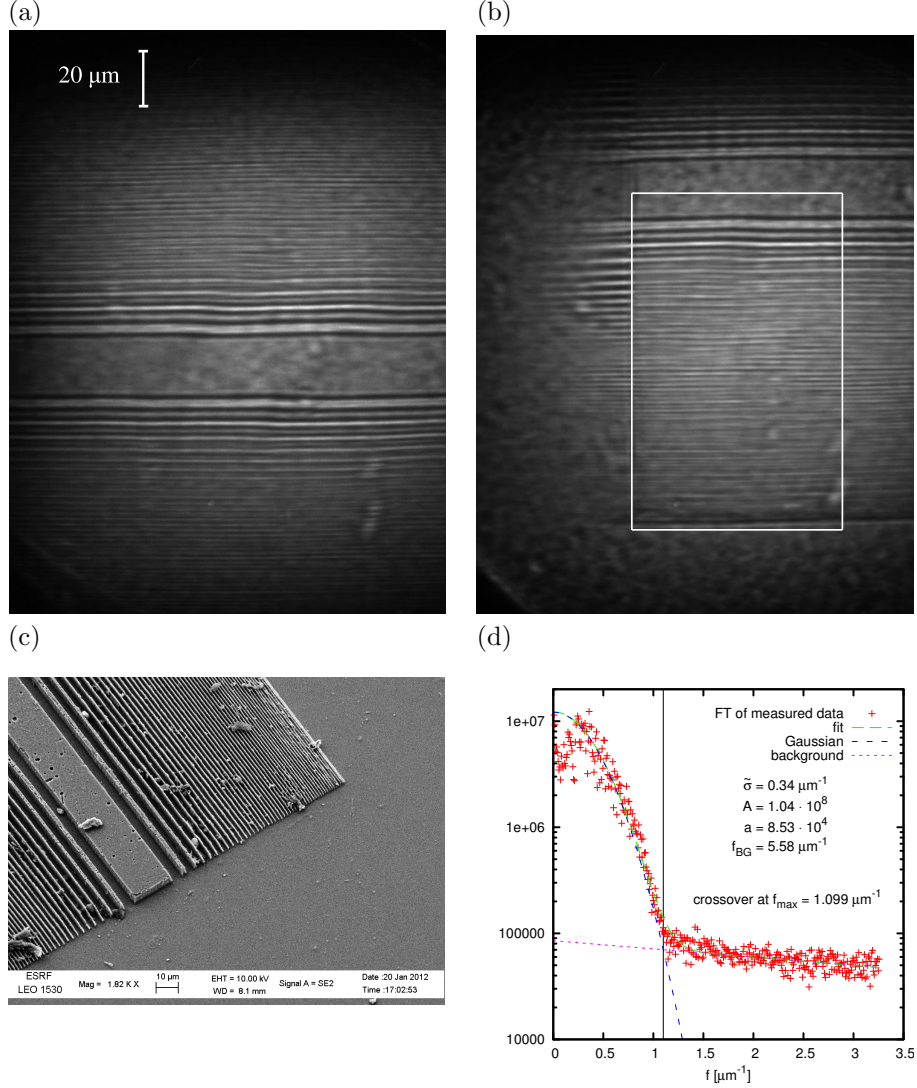


Figure 4: a), b) Diffraction microscopy images of a Bragg-Fresnel lens (Exposure times a) 1 s and b) 2.5 s). c) Scanning electron microscope image of the same Bragg-Fresnel lens. d) Fourier analysis of the stripe structures. The region of interest (ROI) shown in (d) was divided into 10 vertical slices. Each slice was Fourier transformed. The average of the resulting magnitudes were fit to eq. 4. The modulation transfer function intersects the background at $f_{\max} = 1.10 \mu\text{m}^{-1}$, indicating a minimum observable peak-to-valley distance of $1/(2f_{\max}) = 0.46 \mu\text{m}$.

average magnitude of the FT is shown in panel d). A Gaussian MTF with an exponential background was fitted to the average FT, again using the magnification factor of $0.156 \mu\text{m}/\text{px}$ to scale the frequency axis.

$$\tilde{I}(f) = A \cdot g(f) + a \cdot e^{-f/f_{BG}} \quad (4)$$

From the resulting parameters (listed in Fig. 4d) two estimates of the resolution were derived: The standard deviation of the MTF, and the frequency f_{\max} where the MTF falls below the background.

The fit yielded $\tilde{\sigma}_{\text{MTF}} = 0.34 \mu\text{m}^{-1}$ and $f_{\max} = 1.10 \mu\text{m}^{-1}$. The period of a structure at this frequency is $\lambda_{\min} = 1/f_{\max} = 0.92 \mu\text{m}$, so that the smallest observable peak-to-valley valley distance on the sample

is $\lambda_{\min}/2 = 0.46 \mu\text{m}$. The standard deviation of the MTF corresponds to a PSF with standard deviation $\sigma_{\text{PSF}} = 1/(2\pi\tilde{\sigma}_{\text{MTF}}) = 0.47 \mu\text{m}$ and FWHM $1.1 \mu\text{m}$ on the sample (7.1 px on the CCD), slightly better than the estimate obtained above for the SiO_2 stripe pattern.

We have thus shown that our setup reaches sub-micrometer resolution in the vertical direction (perpendicular to the scattering plane). In the horizontal direction (parallel to the scattering plane) the sample does not lie perpendicular to the camera plane. Viewing the sample at the Bragg angle θ_B yields a projected in-plane images size that is smaller by a factor $\sin(\theta_B)$, here $\sin(32.63^\circ) = 0.539$. Assuming that the resolution limit is given by the detector and the diffraction limit of the imaging lenses, the in-plane resolution at the sample surface is then degraded by the factor $1/\sin(\theta_B) = 1.85$ compared to the vertical out-of-plane direction. Furthermore, within the scattering plane, the beam transverses the scatterer partly. The beam path length inside the sample (limited by absorption or extinction) is comparable to the resolution, so that additional blurring is to be expected. This could be avoided in backscattering geometry ($\theta_B \approx 90^\circ$), or when imaging high-Z materials with low penetration depth.

4 Discussion

Using the example of the SiO_2 stripe sample, we now discuss the information obtainable from diffraction images taken at different Bragg angles. We recall that the reflected intensity stems from the underlying single crystalline Si wafer and not from the amorphous top structure of SiO_2 stripes.

Contrast in the diffraction image may arise from several effects: (a) absorption leading to different amplitudes of rays that do or do not travel through the thin SiO_2 layer (b) phase shift between these beams, as the index of refraction of SiO_2 is different from unity, and (c) local variations of the Si(111) reflectivity due to strain in the Si substrate induced by the overlying SiO_2 layer.

For (a) and (b) we can calculate the expected contrast. The index of refraction of SiO_2 at $E = 11 \text{ keV}$ is $n = 1 - \delta + i\beta$ with $\delta = 3.8 \cdot 10^{-6}$ and $\beta = 2.7 \cdot 10^{-8}$ [19], assuming a density of 2.2 g/cm^3 . The path length of the X-rays through SiO_2 is $L = 2z/\sin(\theta_B) = 4.3 \mu\text{m}$. The E-field amplitude of the beam travelling through the SiO_2 layer is therefore reduced to $\exp(-2\pi L\beta/\lambda) = 0.9935$, whereas its phase is shifted by $L\delta/\lambda \cdot 360^\circ = 52^\circ$ as compared to the beam travelling through an adjacent groove via the bare Si surface. Consequently, the absorption contrast (a) is expected to be $1 - \frac{0.9935^2}{1} = 1.3\%$. The phase contrast (b) occurs through interference at the edges. It can be estimated in calculating the intensity resulting from the superposition of two beam parts that travel (i) through the SiO_2 and acquiring the 52° phase shift and a part (ii) that does not travel through the SiO_2 , but through the groove. This intensity is to be compared with the signal from two beams that did not experience a relative phase shift. We obtain a phase contrast of $1 - \frac{|1 + \exp(i \cdot 52^\circ)|^2}{|1 + 1|^2} = 20\%$. For the regular SiO_2 pattern of Fig 2b), the measured contrast was 35%. So a part of the contrast must come from strain.

The magnitude of the strain contrast (c) is difficult to estimate. However, for (a) and (b) the contrast at each point of the rocking curve should be identical, whereas strain might shift and broaden the rocking curve, so that for (c) the contrast in the diffraction micrographs at different points of the rocking curve might differ [14].

This can indeed be seen when comparing images recorded at different positions on the rocking curve (Fig. 2a–d). Fig. 2a and 2b show intensity on the right-hand side of the SiO_2 line pattern, caused by strain propagation beyond the etched areas. Fig. 2c and d show that control structures etched into the SiO_2 (shown in the right part of the SEM image, Fig. 2f) cause strong strain in the Si substrate.

Such shifts of the rocking curve can occur via two routes, local tilting of the lattice planes, or local modifications of the lattice parameter [20, 21]. In the former, a positive tilt on one side of a straining feature should be accompanied by a negative tilt on the opposite side. The corresponding areas should be visible at angles symmetric to the center of the rocking curve. A local modification of the lattice parameter, on the other hand, would lead to a unidirectional shift with respect to the unstrained rocking curve [14].

The sharp features visible in Fig. 2d appear only $\approx 0.009^\circ$ above the rocking curve, indicating that the

lattice parameter is compressed by

$$\frac{\Delta d}{d} \approx \cot(\theta_B) \cdot \Delta\theta \approx 2.5 \cdot 10^{-4}. \quad (5)$$

As shown in Fig. 2e, this strain level is clearly resolved in our experiment. The sensitivity to lattice strain could be further improved by selecting higher order Bragg reflections with narrower rocking curves.

5 Conclusion

X-ray diffraction microscopy combines the advantages of X-ray microscopy in forward scattering geometry and conventional diffraction topography without image magnification:

- As in transmission X-ray microscopy, the effective resolution is greater than that achievable with conventional diffraction topography, which is limited by detector resolution and sample-to-detector distance (diffraction effects).
- As in diffraction topography, the technique is sensitive to microscopic crystallographic imperfections such as strain, dislocations, twinning, etc.

As we have shown here, data acquisition is fast: A single exposure is sufficient and contains all the maximum resolution information, thus the technique is robust with respect to instabilities of the experimental setup, and it has the potential to study transient, non-equilibrium phenomena where it is impossible to acquire several images of the same state.

It should be underlined that the proposed diffraction microscopy technique has great potential for non-destructive studies of highly deformed metals and alloys. By comparing the images taken at different angular settings the contrast due to strain or orientation are easily distinguished [22]. Adding a tomography option (180° rotation) will provide 3D mapping of the orientation and strain of individual grains in polycrystalline materials.

The use of CRLs is of particular interest in diffraction topography since these optics are well adapted to focusing hard X-rays, and are relatively straight-forward to implement on existing diffractometer setups. The technique, however, can also be used with other imaging systems such as Fresnel zone plates [14, 13] or mirrors such as Wolter optics [23, 24]. This flexibility enables the use of X-ray diffraction microscopy over a very wide range of photon energies from sub-keV soft X-rays, e.g. for the study of multilayers, to very hard X-rays with several tens of keV. Furthermore, the technique can be combined with other standard X-ray techniques to access information unobtainable in transmission geometry. Examples include grazing-incidence diffraction to image micro- and nanostructures grown on a surface, magnetic scattering to image ferromagnetic [25] or antiferromagnetic [26] magnetic domain patterns and the imaging of ferroelectric domains [27].

Finally, the field of view and the magnification can be adjusted in-situ simply by changing the number of lenses (e.g. by using a Transfocator) and the sample-to-lens or lens-to-detector distance.

Acknowledgments

We acknowledge the European Synchrotron Radiation Facility (ESRF) for the provision of beam time on ID06. C. D. thanks R. Barrett for stimulating discussions and critical reading of the manuscript.

References

- [1] W Berg, “Über eine röntgenographische Methode zur Untersuchung von Gitterstörungen an Kristallen”, *Naturwissenschaften* 19 (1931), p. 391.
- [2] C. S. Barrett, “Laue spots from perfect, imperfect and oscillating crystals”, *Phys. Rev.* 38 (1931), p. 832.

- [3] C. S. Barrett, “A new microscopy and its potentialities”, *Trans. AIME* 161 (1945), p. 15.
- [4] G. Ramachandran, “X-Ray topographs of diamond”, *Proc. Math. Sci.* 19 (1944), p. 280.
- [5] T. Martin and A. Koch, “Recent developments in X-ray imaging with micrometer spatial resolution”, *Journal of Synchrotron Radiation* 13.2 (2006), p. 180.
- [6] P. Kirkpatrick and A. V. Baez, “Formation of Optical Images by X-Rays”, *J. Opt. Soc. Am.* 38 (1948), p. 766.
- [7] A. V. Baez, “A Study in Diffraction Microscopy with Special Reference to X-Rays”, *J. Opt. Soc. Am.* 42 (1952), p. 756.
- [8] J. H. Underwood, T. W. Barbee Jr., and C. Frieber, “X-ray microscope with multilayer mirrors”, *Appl. Opt.* 25.11 (1986), p. 1730.
- [9] B. Lai et al., “Development of a hard x-ray imaging microscope”, *Rev. Sci. Instrum.* 66 (1995), p. 2287.
- [10] A. Snigirev et al., “High energy X-ray phase contrast microscopy using a circular Bragg-Fresnel lens”, *Optics Communications* 135.46 (1997), p. 378.
- [11] B. Lengeler et al., “Imaging by parabolic refractive lenses in the hard X-ray range”, *J. Synchrotron Rad.* 6 (1999), p. 1153.
- [12] A. Bosak et al., “High-Resolution Transmission X-ray Microscopy: A New Tool for Mesoscopic Materials”, *Advanced Materials* 22.30 (2010), pp. 3256–3259.
- [13] P. Fenter et al., “Observation of subnanometre-high surface topography with X-ray reflection phase-contrast microscopy”, *Nature Phys.* 2 (2006), p. 700.
- [14] R. Tanuma and T. Kubo, “Fresnel-Zone-Plate-Magnified X-ray Topography”, *Jpn. J. Appl. Phys.* 45 (2006), p. 5280.
- [15] S. Matsuyama et al., “Hard-X-ray imaging optics based on four aspherical mirrors with 50 nm resolution”, *Opt. Express* 20.9 (2012), pp. 10310–10319.
- [16] J. Chavanne, C. Penel, and P. Elleaume, “Development and Operation of a Prototype Cryogenic Permanent Magnet Undulator at the ESRF”, *Synchrotron Rad. News* 22 (4 2009), p. 34.
- [17] V. Aristov et al., “Bragg zone plates for hard X-ray focusing”, *Nucl. Instrum. Meth. Phys. Res. A* 261 (1987), p. 72.
- [18] S. Kuznetsov et al., “A linear single-crystal Bragg-Fresnel lens with SiO₂ surface structure”, *AIP Conf. Proc.* 705 (2004), p. 744.
- [19] CXRO, the center for X-ray optics, http://henke.lbl.gov/optical_constants, Lawrence Berkeley National Laboratory, Materials Sciences Division.
- [20] V. V. Aristov et al., “Possibilities of x-ray interference diffractometry for the reconstruction of two-dimensional lattice deformation profiles in crystals”, *Semicond. Sci. Technol.* 7 (1992), p. 1109.
- [21] V. Aristov et al., “X-ray diagnostics of 2D strain profiles in semiconductor crystals”, *Semicond. Sci. Technol.* 7 (1992), A168.
- [22] A. M. Afanas’ev and V. G. Kohn, “Dynamical theory of X-ray diffraction in crystals with defects”, *Acta Cryst. A* 27 (1971), p. 421.
- [23] H. Wolter, “Spiegelsysteme streifenden Einfalls als abbildende Optiken für Röntgenstrahlen”, *Ann. Phys.* 445 (1952), p. 94.
- [24] H. Takano et al., “X-ray scattering microscope with a Wolter mirror”, *Rev. Sci. Instrum.* 72 (2002), p. 2629.
- [25] A. Kreyssig et al., “Probing Fractal Magnetic Domains on Multiple Length Scales in Nd₂Fe₁₄B”, *Phys. Rev. Lett.* 102 (2009), p. 047204.
- [26] J. C. Lang et al., “Imaging spiral magnetic domains in Ho metal using circularly polarized Bragg diffraction”, *J. Appl. Phys.* 95 (2004), p. 6537.

- [27] G. Fogarty et al., “Antiparallel ferroelectric domains in photorefractive barium titanate and strontium barium niobate observed by high-resolution x-ray diffraction imaging”, *J. Opt. Soc. Am. B* 13 (1996), p. 2636.